





Formation of $\text{Ni}_x\text{Fe}_{3-x}\text{O}_4$ on $\text{Fe}_3\text{O}_4(001)$ Mert Taskin ¹, Zbynek Novotny ^{1,2,3}, Matthias Hengsberger ¹, and Jürg Osterwalder ^{1,*}¹Physik-Institut, Universität Zürich, Winterthurerstrasse 190, CH-8057, Zürich, Switzerland²Swiss Light Source, Paul-Scherrer-Institut, CH-5232 Villigen, Switzerland³EMPA, Laboratory for Joining Technologies and Corrosion, Swiss Federal Laboratories for Materials, CH-8600 Dübendorf, Switzerland

(Received 1 November 2022; revised 22 February 2023; accepted 12 April 2023; published 1 May 2023)

Magnetite (Fe_3O_4) doped with earth-abundant metals has become a promising catalyst material. In particular, Ni-doped magnetite ($\text{Ni}/\text{Fe}_3\text{O}_4$) has been demonstrated as a cheap, robust, and catalytically active material in photocatalytic and electrochemical water oxidation. Recently, the incorporation of Ni atoms in Fe_3O_4 single crystalline surfaces was studied extensively with scanning tunneling microscopy and density-functional theory calculations. However, because of its importance for catalytic activity, this incorporation process and the determination of the lattice sites occupied by the Ni atoms require further experimental study. In this work, we investigated the surface structure of as-grown and annealed $\text{Ni}/\text{Fe}_3\text{O}_4(001)$ as a function of Ni coverage under ultra-high vacuum conditions with temperature-dependent x-ray and ultraviolet photoelectron spectroscopy, x-ray photoelectron diffraction, and low-energy electron diffraction. We observe that octahedrally coordinated subsurface cation vacancy sites are already occupied upon Ni deposition at room temperature and that Ni atoms start to diffuse further into the octahedral subsurface sites with increasing temperature.

DOI: [10.1103/PhysRevMaterials.7.055801](https://doi.org/10.1103/PhysRevMaterials.7.055801)

I. INTRODUCTION

Photoelectrochemical cells (PECs) for water splitting have been attracting attention in the search of a method to store clean and renewable energy coming from the sun in the form of chemical energy. The most common configuration consists of two semiconducting electrodes—one for water reduction (photocathode) and one for water oxidation (photoanode)—where photons are absorbed and subsequently converted into electron-hole pairs. However, investigations have shown that high-performance photoelectrodes can be obtained only by employing expensive semiconductors and noble-metal catalysts [1]. Thus, searching for new cheap materials or increasing the efficiency and stability of those already studied is mandatory to boost PEC performance and their application. Among earth-abundant materials, magnetite (Fe_3O_4) was found to be a promising substrate for catalytic water oxidation and reduction due to its chemical stability in aqueous solutions [2]. Spinel-type ferrites ($\text{M}_x\text{Fe}_{3-x}\text{O}_4$) can be derived from Fe_3O_4 by doping with divalent cations (M) [3]. These structures can have suitable band alignment with the redox potential of water, suggesting an efficient charge transfer at the solid-liquid interface. In particular, Ni-doped magnetite ($\text{Ni}/\text{Fe}_3\text{O}_4$) turned out to be a cheap, robust, and

catalytically active surface as observed in photocatalytic [4] and electrochemical [5] water oxidation.

Fe_3O_4 has an inverse spinel crystal structure with $\text{Fd}\bar{3}m$ space group above 120 K where the so-called Verwey transition occurs [7]. In the high-temperature structure, oxygen anions form a face-centered cubic lattice with Fe^{3+} and Fe^{2+} cations on tetrahedral and octahedral sites (see Fig. 1). Half of the Fe^{3+} cations occupy tetrahedral sites ($\text{Fe}_{\text{tet}}^{3+}$) (silver), while the other half occupy octahedral sites ($\text{Fe}_{\text{oct}}^{3+}$) (brown) along with an equal number of Fe^{2+} cations ($\text{Fe}_{\text{oct}}^{2+}$) (also brown), resulting in the overall chemical composition $(\text{Fe}_{\text{oct}}^{2+})(\text{Fe}_{\text{oct}}^{3+})(\text{Fe}_{\text{tet}}^{3+})(\text{O}^{2-})_4$. The clean $\text{Fe}_3\text{O}_4(001)$ surface displays a $(\sqrt{2} \times \sqrt{2})\text{-R}45^\circ$ surface reconstruction, where two Fe_{oct} vacancies and one interstitial $\text{Fe}_{\text{tet}}^{\text{int}}$ defect per unit cell form in the second (S-2) and first (S-1) subsurface layer, respectively [8] (see Fig. S11 of the Supplemental Material [9]). Each reconstructed surface unit cell offers one particularly stable adsorption site for metal atoms in a twofold coordination at the position where there is no extra Fe_{tet} in the (S-1)st layer. One of the vacant subsurface sites in (S-2) can be readily occupied by a guest cation. However, the presence of the $\text{Fe}_{\text{tet}}^{\text{int}}$ defect blocks the adsorption of a second cation within the same reconstructed cell [5]. Incorporation of divalent cations into the crystal to form ferrite-like structures restores the crystal termination from a $(\sqrt{2} \times \sqrt{2})\text{-R}45^\circ$ reconstructed to a bulk-truncated $p(1 \times 1)$ surface by filling one of the two vacant sites while the other one is occupied by the adjacent $\text{Fe}_{\text{tet}}^{\text{int}}$.

The adsorption and incorporation of transition metals such as Ni [5,10,11], Ag [12], Au [13], or Pd [14] on $\text{Fe}_3\text{O}_4(001)$ were studied extensively with surface characterization methods. Electrochemical measurements taken with different coverages for the $\text{Ni}/\text{Fe}_3\text{O}_4(001)$ surface showed

*juerg.osterwalder@physik.uzh.ch

that the amount of Ni incorporated into the substrate can tune the water oxidation efficiency [5]. A low coverage (<1 ML) the Ni deposition on the reconstructed surface at room temperature was reported to lead to Ni adsorption in twofold coordinated adatom sites in the chemical state Ni^{1+} . In a combined x-ray photoelectron spectroscopy (XPS) and scanning-tunneling microscopy (STM) study, Bliem *et al.* could show that a following postannealing of the samples at 465 K induced the transformation to a higher oxidation state (Ni^{2+}) accompanied by a change in the structural arrangement suggesting the incorporation of Ni into the surface [8]. Moreover, the positions of Ni atoms after their adsorption and incorporation into the reconstructed $\text{Fe}_3\text{O}_4(001)$ surface were investigated by the normal incidence x-ray standing wave (NIXSW) technique. It was found that Ni adatoms adsorb at a height of 0.46 Å above the topmost Fe_{oct} layer, and that incorporated Ni atoms occupy Fe_{oct} subsurface sites [11].

Since initial water adsorption is governed by surface Ni sites [15], the distribution of Ni near the surface layers of a highly doped $\text{Ni}/\text{Fe}_3\text{O}_4$ (>1 ML) is a key parameter for searching the best dopant concentration in view of the most efficient water oxidation catalysis. Therefore, in the present study we focus on the structure of large coverages of Ni on magnetite which are found to be close to ferrite-like $\text{Ni}_x\text{Fe}_{3-x}\text{O}_4(001)$ ($x > 1$) surfaces. As-grown and postannealed $\text{Ni}/\text{Fe}_3\text{O}_4(001)$ samples for two different Ni coverages under ultra-high vacuum (UHV) conditions are used for investigating the chemical kinetics of the Ni incorporation by temperature-dependent photoelectron spectroscopy and the transformation of $\text{Ni}_x\text{Fe}_{3-x}\text{O}_4(001)$ from $x = 1$ to $x = 2$. Eventually, as a complementary technique to NIXSW, x-ray photoelectron diffraction (XPD) was used to probe the Ni distribution on-top of and within the subsurface layers and to identify the lattice sites of the incorporated Ni atoms.

II. EXPERIMENTAL DETAILS

Naturally occurring $\text{Fe}_3\text{O}_4(001)$ single crystals (SurfaceNet GmbH) were used in our experiments. The data were acquired from two different equivalent samples. All data sets were found to be consistent between the two samples. To obtain the reconstructed surface, the pristine $\text{Fe}_3\text{O}_4(001)$ samples were prepared with two cycles of Ar^+ sputtering with an acceleration potential $U_{\text{acc}} = 0.45$ kV (10 min) and annealing ($T = 950$ K) under an oxygen pressure of $p_{\text{O}_2} = 5 \times 10^{-7}$ mbar (20 min). Ni wire (Alfa Aesar, 99.999%) of 2 mm diameter was used to deposit Ni films on $\text{Fe}_3\text{O}_4(001)$ surfaces with an e-beam evaporator (Ferrovac GmbH). The evaporation rate of Ni was calibrated on a clean polycrystalline Cu-foil (Alfa Aesar) by means of normal-emission XPS signals with the following equation (see Refs. [16,17] and Sec. III for details):

$$d_{\text{Ni}} = -\lambda_{\text{Ni}} \ln \left(1 - \frac{I_{\text{Ni}} n_{\text{Cu}} \sigma_{\text{Cu}} \lambda_{\text{Cu}}}{I_{\text{Cu}} n_{\text{Ni}} \sigma_{\text{Ni}} \lambda_{\text{Ni}}} e^{-\frac{d_{\text{Ni}}}{\lambda_{\text{Ni}} (E_{\text{kin}}^{\text{Cu}})}} \right), \quad (1)$$

where d_{Ni} is the Ni thickness, I_X is the photoemission intensity from a core level of element X ($X = \text{Ni}, \text{Cu}$), n_X is the three-dimensional atomic density, σ_X is the photoionization cross-section [18], λ_X is the inelastic-mean-free path (IMFP) of photoelectrons in material X with kinetic energy E_{kin}^Y

(kinetic energy omitted when $Y = X$), as calculated with the predictive Tanuma-Powell-Penn (TPP-2M) formula [19]. We use the monolayer coverage definition (1 ML := 1 Ni atom per $(\sqrt{2} \times \sqrt{2})\text{-R}45^\circ$ surface unit cell area) introduced by Bliem *et al.* [10] and applied a deposition rate of $\Gamma = 2.26$ ML/min, where $1 \text{ ML} \approx 1.4 \times 10^{14}$ Ni atoms cm^{-2} .

Based on electrochemical measurements under oxygen evolution, the $\text{Ni}/\text{Fe}_3\text{O}_4(001)$ system showed the highest catalytically active and stable surface after Ni deposition to a total coverage of 50 ML, which was administered in sequential 2 ML amounts at room temperature, followed each time by a mild annealing to 473 K in order to ensure incorporation of Ni atoms into subsurface lattice sites [5]. Under these conditions, the composition of the surface layer was quantified to be $\text{Fe} : \text{Ni} = 40 : 60$ as determined by low-energy ion scattering. To investigate the adsorption and incorporation mechanisms, we kept our Ni depositions at lower coverages: 1 ML at room temperature and 26 ML at 473 K, followed by postannealing at 607 K. The former provides more information related to the adsorption of Ni and the initial incorporation step. On the other hand, the latter offers a better signal for examining the formation of the Ni-ferrite-like structure upon postannealing. Note that with the above definition of the monolayer, the 26 ML coverage corresponds to the equivalent amount of only 2.3 dense layers of Ni, assuming a $\text{Ni}(001)$ orientation.

XPS measurements were conducted in a modified VG ESCALAB 220 UHV system with a base pressure of 2.1×10^{-10} mbar. To probe the core-level electrons, the sample was irradiated with nonmonochromatized $\text{Mg } K_\alpha$ ($\hbar\omega = 1253.6$ eV) or $\text{Si } K_\alpha$ ($\hbar\omega = 1740$ eV) radiation from a twin anode x-ray source. All XPS spectra (including those taken at varying temperatures) were acquired at normal emission $\theta = 0^\circ$ using a constant solid angle Ω with the conical analyzer acceptance angle set to an opening angle of $\Delta\theta \leq \pm 3^\circ$ [20], and a pass energy $E_{\text{pass}} = 50$ eV. A monochromatized microwave-driven high flux He discharge lamp ($\text{He } I_\alpha$, $\hbar\omega = 21.22$ eV) was used for the valence-band measurements (Gammadata Burkli AB, Sweden). The photoelectrons were counted in the analyzer by six channeltrons sitting at slightly different energies. The energy scale of the electron analyzer for XPS measurements was calibrated as described by Seah *et al.* [21]. For UPS measurements, the calibration was made based on the position of the Fermi level measured on freshly prepared polycrystalline silver. Temperature-dependent photoemission spectra were obtained with gated resistive heating as described by Kreutz *et al.* [22]. Briefly, an alternating current was applied to a tungsten filament located beneath the sample holder to regulate the temperature. The data acquisition was gated during heating cycles and both cycles heating and data acquisition alternated every second. The temperature calibration was carried out using a K-type thermocouple in direct thermal contact with the Mo sample holder and under the same conditions (duty cycle times and filament current) as used during the photoemission experiments.

XPD patterns were obtained by measuring the angular intensity distributions of the $\text{Fe } 2p_{3/2}$ and $\text{O } 1s$ photoelectrons, as well as the Ni LMM Auger line. The typical total measurement time for a XPD pattern ranges between 3.5 and 7 hours depending on the number of angular manipulator settings. These patterns were recorded as a function of azimuthal

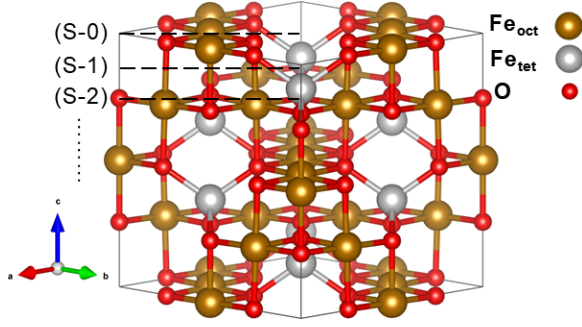


FIG. 1. The crystal structure of Fe_3O_4 . Solid black lines correspond to the $(\sqrt{2} \times \sqrt{2})\text{-R}45^\circ$ unit cell with a lattice constant 8.44 Å [6]. Dashed lines indicate the top three layers [(S-0), (S-1), (S-2)] with the layer indexing convention labeled on the left. Tetrahedrally and octahedrally coordinated Fe are given in silver and brown atoms, respectively.

($\phi = 0^\circ$ to 360°) and polar angles ($\theta = 80^\circ$ to 0°) at constant kinetic energy after the subtraction of the inelastic background [23,24]. A Gaussian-shaped polar background was subtracted from each pattern in order to account for purely instrumental intensity variations. Fourfold symmetrical rotational averaging was applied to the XPD patterns in order to improve the statistical accuracy, but all features were also clearly visible in the nonsymmetrized data.

III. COMPUTATIONAL DETAILS

The temperature-dependent XPS data from the 26 ML $\text{Ni}/\text{Fe}_3\text{O}_4(001)$ system indicated the formation of three-dimensional (3D) metallic Ni clusters (Ni^0) on the as-grown sample that progressively dissolved during the postannealing.

To track the temperature evolution of $\text{Ni } 2p_{3/2}$ signals, originating from Ni^{2+} ions incorporated in the substrate lattice, and from Ni^0 atoms in the clusters (Fig. 2) we used the following set of equations to determine the average density n_X^{sub} . Thereby, it was assumed that the ions in the substrate were continuously distributed, and any variations in cluster shape were neglected. The x-ray photoelectron current per sample area from a layer of thickness dz at depth z into a constant solid angle for an element and oxidation state X in

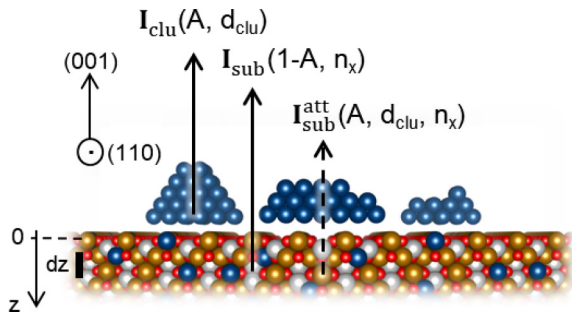


FIG. 2. Model of the excess Ni^0 clusters which form at relatively high coverages of Ni on $\text{Fe}_3\text{O}_4(001)$. The different contributions to the photoemission intensity I are indicated (Ni, Fe_{oct} , Fe_{tet} , and O atoms in blue, brown, silver, and red, respectively).

a semi-infinite material is given by [24]

$$dI_X(z) = n_X \sigma_X T(E_{\text{kin}}^X) \exp\left(-\frac{z}{\lambda_X(E_{\text{kin}}^X) \cos(\theta)}\right) dz, \quad (2)$$

where $T(E_{\text{kin}}^X)$ is analyzer transmission function and θ denotes the polar angle. Neglecting the instrumental parameters, the integrated photoelectron intensity for normal emission ($\theta = 0^\circ$) is proportional to

$$I_X \propto n_X \sigma_X \lambda_X(E_{\text{kin}}^X). \quad (3)$$

The photoelectrons are scattered by neighboring atoms leading to an angle-dependent intensity modulation, which is called a photoelectron diffraction pattern [24]. When comparing intensities of different elements at different sites, which were measured in a fixed solid angle and at a fixed polar emission angle, these diffraction effects must be considered because they may alter the intensity ratios between different elements. We investigated the diffraction effects for the different core levels used to retrieve the composition of the samples. It turns out that the metal-to-oxygen ratio is underestimated by about 14%–20% if these effects are not taken into account. Therefore, in this paper we corrected the XPS intensity ratios for the diffraction effects in normal emission.

When 3D clusters form on a surface with an average fractional coverage A ($1 \geq A \geq 0$) and thickness d_{clu} , the spectral intensity from the substrate in the covered area is reduced by an inelastic attenuation factor:

$$I_{\text{sub}}^{\text{att}} \propto A n_X^{\text{sub}} \sigma_X \lambda_X(E_{\text{kin}}^X) \exp\left(\frac{-d_{\text{clu}}}{\lambda_{\text{clu}}(E_{\text{kin}}^X)}\right), \quad (4)$$

where n_X^{sub} is rewritten with the superscript to distinguish from the atomic density of metallic Ni atoms in the cluster n_{clu} . The cluster-free surface area contributes to the signal according to the following proportionality:

$$I_{\text{sub}} \propto (1 - A) n_X^{\text{sub}} \sigma_X \lambda_X(E_{\text{kin}}^X), \quad (5)$$

and the overall intensity becomes

$$I_{\text{sub}}^{\text{tot}} = I_{\text{sub}}^{\text{att}} + I_{\text{sub}}. \quad (6)$$

Likewise, the integrated intensity from the clusters can be written as

$$I_{\text{clu}} \propto A n_{\text{clu}} \sigma_{\text{clu}} \lambda_{\text{clu}}(E_{\text{kin}}^{\text{clu}}) \left[1 - \exp\left(\frac{-d_{\text{clu}}}{\lambda_{\text{clu}}(E_{\text{kin}}^{\text{clu}})}\right)\right]. \quad (7)$$

Identifying element X with either Ni^{2+} or oxygen and the clusters with Ni^0 , the spectral intensity ratios between the substrate and cluster emission were modeled and compared with our temperature-dependent XPS data to determine the approximate values of A , d_{clu} , and the density n_X^{sub} (see Figs. SI2 through SI6 of the Supplemental Material [9] for a detailed description of the procedure).

Simulations of XPD patterns were obtained with the electron diffraction in atomic clusters (EDAC) code [25]. For these simulations, atomic clusters were set up that represent the bulk truncated $p(1 \times 1)$ and the reconstructed $(\sqrt{2} \times \sqrt{2})\text{-R}45^\circ$ structures along a (001) plane. To interpret the measured Ni LMM Auger diffraction data, layer-resolved XPD patterns for $\text{Fe } 2p_{3/2}$ were simulated by selecting Fe emitters [6] in the

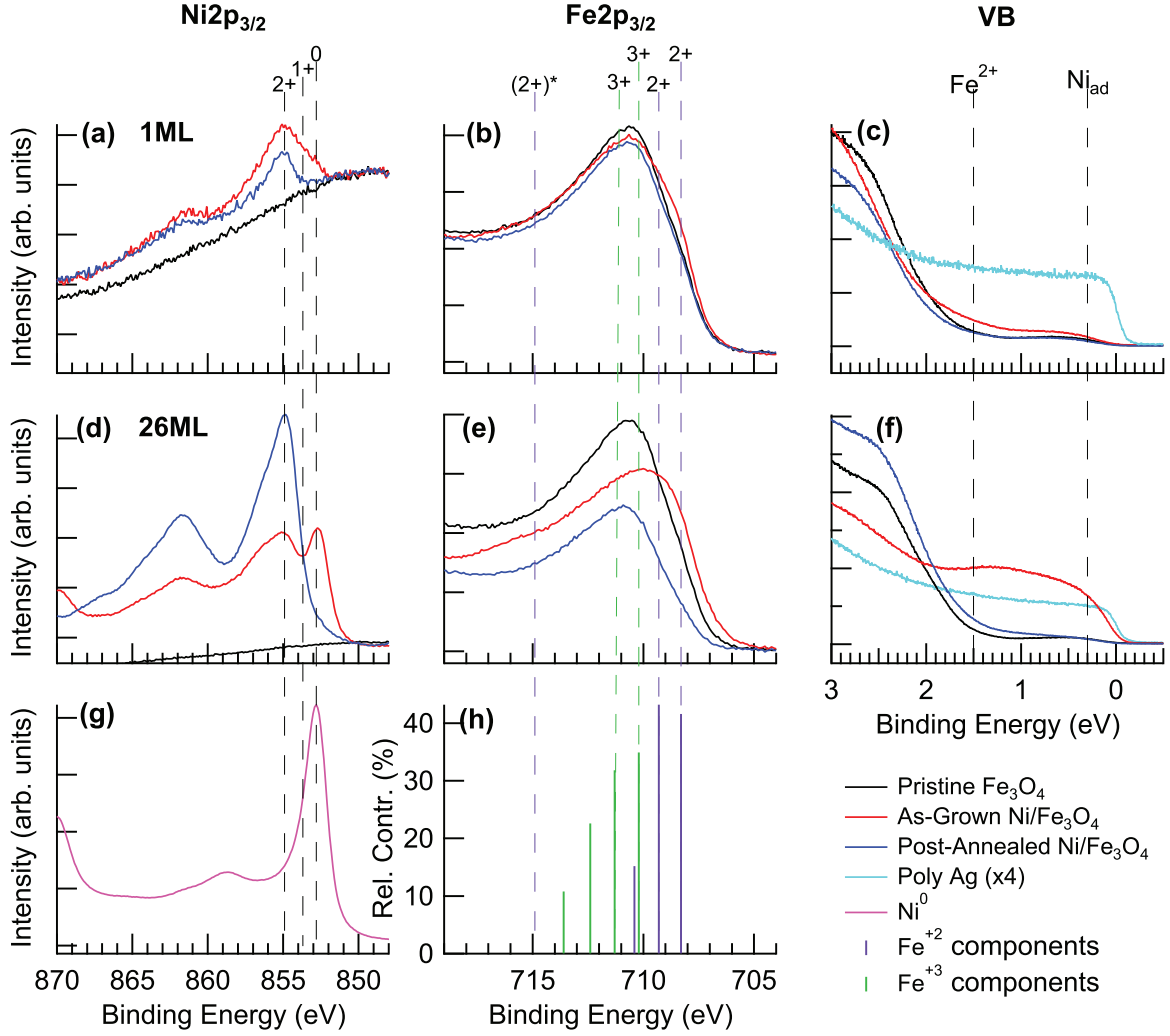


FIG. 3. Photoelectron spectra of (a), (d) Ni $2p_{3/2}$, (b), (e) Fe $2p_{3/2}$, (c), (f) valence (VB) regions acquired from 1 ML (top row) and 26 ML (middle row) Ni/Fe₃O₄(001). Black, red, and blue spectra indicate spectra that were taken from the pristine sample, the as-grown and the postannealed films, respectively. (g) The Ni $2p_{3/2}$ spectrum from Ni metal is used as reference for the Ni⁰ line position. The $2p$ binding energies corresponding to the Ni¹⁺ and Ni²⁺ oxidation states are shown with dashed vertical lines at 853.7 and 855 eV, respectively [10]. (h) Relative contributions of the multiplet peaks calculated for the Fe²⁺ components; the label * refers to a shake-up satellite of the specified component [31]. Core-level spectra were measured with Mg K_{α} ($\hbar\omega = 1253.6$ eV), valence-band spectra with He I_{α} ($\hbar\omega = 21.22$ eV) light. The spectra of each panel were shifted vertically such that the background signal at the low-binding-energy side of the match that of the pristine sample for the sake of comparison.

surface or in the ($S-n$)th subsurface layer but with the kinetic energy of the Ni LMM Auger line at 840 eV. At these energies the XPD patterns are dominated by forward scattering along the nearest-neighbor directions and do not depend strongly on the emission process [26]. In some cases, a quantitative comparison between experimental and simulated XPD patterns is given by using the Pendry reliability factor (R factor) [27,28]:

$$R = \frac{\sum_i [\chi_{\text{cal}}^i(\theta, \phi) - \chi_{\text{exp}}^i(\theta, \phi)]^2}{\sum_i \chi_{\text{cal}}^i(\theta, \phi)^2 + \chi_{\text{exp}}^i(\theta, \phi)^2} \quad (8)$$

where χ_{cal} and χ_{exp} are simulated and experimental XPD modulation functions, respectively, and the summation over i runs over all discrete angular positions (θ, ϕ). The modulation function $\chi(\theta, \phi)$ is obtained from the intensities $I(\theta, \phi)$ by first calculating a strongly smoothed function $I_0(\theta, \phi)$ via

locally weighted scatter-plot smoothing (LOESS) and then forming $\chi = (I - I_0)/I_0$.

Finally, the crystal structures were drawn with VESTA 3 software [29].

IV. RESULTS AND DISCUSSION

Figure 3 shows photoelectron spectroscopy results from as-grown and postannealed Ni-films up to 607 K on ($\sqrt{2} \times \sqrt{2}$)-R45° Fe₃O₄(001) surfaces with 1 ML [Figs. 3(a)–3(c)] and 26 ML [Figs. 3(d)–3(f)] coverages. A measurement taken on metallic Ni [Fig. 3(g)] and the relative contributions of the multiplet peaks calculated for the Fe²⁺ components [30] [Fig. 3(h)] are shown as a reference.

For 1 ML coverage, the Ni $2p_{3/2}$ spectrum for the as-grown film [Fig. 3(a), red] shows a broad peak with its maximum at

854.9 eV. There is a shoulder at lower binding energy, which suggests that Ni adsorption occurs in several chemical states. According to DFT + U calculations [10], the chemical state of Ni depends on the adsorption site on $\text{Fe}_3\text{O}_4(001)$. A binding energy of 855 eV corresponds to Ni^{2+} ions that occupy the octahedral site with either a Fe_{oct} substitution in the surface layer [$\text{Ni}_{\text{oct}}(\text{S})$] or filling one of the vacant sites in the (S-2)nd layer [$\text{Ni}_{\text{oct}}(\text{S-2})$]. Moreover, a Ni^{1+} state can be found with a binding energy of 853.7 eV, associated with adatoms in a twofold coordination (Ni_{ad}). The energetically most favorable configurations are reported as $E_{\text{Ni}_{\text{oct}}(\text{S-2})} > E_{\text{Ni}_{\text{ad}}} > E_{\text{Ni}_{\text{oct}}(\text{S})}$, while Ni occupation of tetrahedral sites is unfavorable. The spectrum for the as-grown 1 ML film in Fig. 3(a) is thus in excellent agreement with the findings of Bliem *et al.* [10], and the shoulder at lower binding energy can be referred to as Ni_{ad} (Ni^{1+}), while that at higher binding energy corresponds to Ni_{oct} (Ni^{2+}). The shoulder around the Ni^{1+} position is rather broad, and it overlaps with the Ni^0 line position (see dashed vertical lines). Ni cluster formation cannot be completely excluded as the surface energy of Ni [32] is higher than that of $\text{Fe}_3\text{O}_4(001)$ [33], but is rather unlikely at this low coverage. Indeed, the peak shape for the Ni^{1+} chemical state can include strong many-body effects due to the multiplet splitting between the $2p$ core hole and unpaired spins in the $3d^9$ shell, leading to peak broadening [34]. On the other hand, there is a satellite peak appearing at the higher binding energy. The distance between main and satellite peaks is measured to be 6.6 eV, which agrees with the reported value for NiFe_2O_4 [35].

Postannealing the sample up to 607 K [Fig. 3(a), blue] changes the relative weight of these two chemical states. The Ni_{ad} atoms essentially disappear due to the incorporation process activated by interdiffusion, resulting in Ni_{oct} becoming the sole component in the spectrum. The overall intensity drops after the postannealing because the subsurface Ni^{2+} cations suffer inelastic attenuation.

The characteristic strong multiplet splitting of Fe $2p_{3/2}$ for the Fe^{2+} and the Fe^{3+} charge states leads to a rather broad spectrum [Fig. 3(b)]. The spectra for all preparations could be well fit with reported positions of multiplet components [31] with slightly varied weights within the Fe^{2+} and the Fe^{3+} manifolds (see Figs. SI7 and SI8 [9]). From these fits the $\text{Fe}^{3+}/\text{Fe}^{2+}$ ratio can be quantified rather precisely. Compared with the pristine spectra, a small but significant change was observed for as-grown 1 ML Ni [Fig. 3(b)] at the lower binding-energy side, indicating an increase of the Fe^{2+} components (see dashed vertical lines). It is known that the concentration of Fe^{3+} cations is enriched at the pristine reconstructed surface [8] as a consequence of the octahedral cation vacancies in the (S-2) layer that are formed predominantly by removal of Fe^{2+} ions. The incorporation of Ni^{2+} ions into octahedral sites leads to a reduction of Fe^{3+} to Fe^{2+} and thereby to the observed increase of the latter component. Interestingly, this effect is reversed upon postannealing suggesting a temperature induced exchange of charges in the surface region, leading to a slightly lower Fe^{2+} concentration than in the pristine surface (see Fig. SI7 [9]). This is to be expected since the incorporation of Ni locally lifts the reconstruction, and Ni^{2+} substitutes Fe^{2+} rather than Fe^{3+} . In the VB region [Fig. 3(c)], the photoemission intensity from the

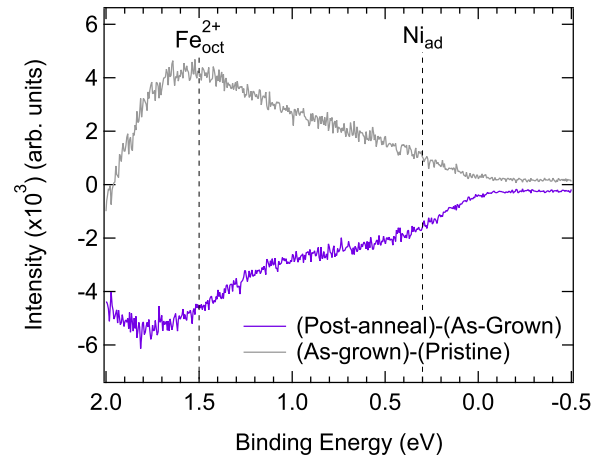


FIG. 4. Valance band spectra differences between “Postannealed” and “As-grown” (purple) and “As-grown” and “Pristine”(gray) taken before or after specified experiment for 1 ML Ni/ $\text{Fe}_3\text{O}_4(001)$. The deposition temperature was room temperature, the postannealing temperature was 607 K. Vertical dashed lines indicate the positions of Ni_{ad} (0.3 eV) [10] and $\text{Fe}_{\text{oct}}^{2+}$ (1.5 eV) [30], respectively.

as-grown sample increases right below E_F with respect to the pristine spectrum. The spectral difference between as-grown and pristine (red-black) reaches a local maximum around 1.5 eV below E_F (Fig. 4). The maximum position is very close to the calculated [30] and measured [36] position of the e_g orbital populated by spin-up $\text{Fe}_{\text{oct}}^{2+}$ electrons. Moreover, it was shown that the presence of Ni_{ad} causes a significant change in the band structure, contributing to density of states (DOS) at around 0.3 eV below E_F [10]. These changes are thus fully in line with the observations in the Ni $2p_{3/2}$ and Fe $2p_{3/2}$ spectra [Figs. 3(a) and 3(b)]. Considering that $\text{Fe}_{\text{oct}}^{3+}$ occupies states more than (≥ 3 eV) below E_F [30,36,37], the observed changes can be attributed to $\text{Fe}_{\text{oct}}^{2+}$ and Ni_{ad} . The changes are in good agreement with the DOS calculations for Ni_{ad} on reconstructed $\text{Fe}_3\text{O}_4(001)$ [10]. The spectral difference between the postannealed and as-grown samples (purple) shows an almost opposite behavior, i.e., a complete removal of the Ni_{ad} states right below E_F and a reduction of intensity around the position of the $\text{Fe}_{\text{oct}}^{2+}$ e_g orbital.

For the 26 ML sample Ni was deposited at 473 K to activate the incorporation process during the growth. The Ni $2p_{3/2}$ spectra of as-grown films show two distinct peaks at 854.9 and 852.8 eV [Fig. 3(d)]. Comparison with the spectrum taken from Ni metal [Fig. 3(g)] leads one to associate the lower binding energy peak to the presence of Ni^0 at the surface. This suggests that some excess amount of Ni accumulates in the form of metallic clusters. Postannealing at 607 K removes the metallic component completely while the Ni^{2+} signal increases, revealing the diffusion of Ni into the subsurface. At the same time a strong feature grows at 861.5 eV, contributing to a Ni $2p_{3/2}$ spectrum that is characteristic of Ni ferrite [35]. The overall Ni $2p_{3/2}$ intensity increases significantly upon postannealing in spite of the diffusion of Ni ions into the substrate that goes along with the formation of a ferrite-like structure. This suggests that the surface of

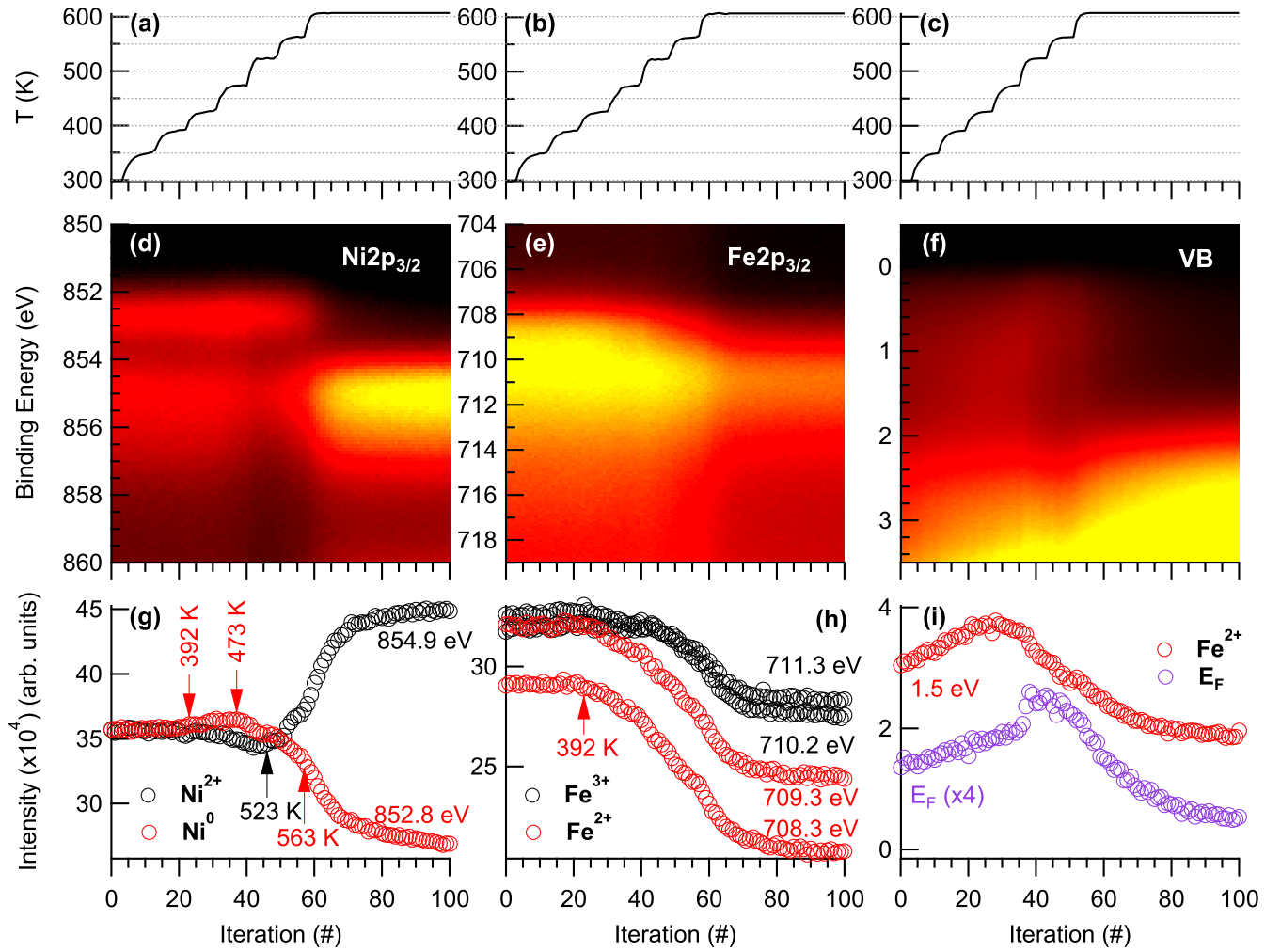


FIG. 5. Postannealing process of a 26 ML Ni/Fe₃O₄(001) sample, investigated with temperature-dependent XPS. (a)–(c) Temperature profiles of the (d) Ni 2p_{3/2}, (e) Fe 2p_{3/2}, (f) VB region heat maps. The yellow-hot color scale represents the photoemission intensity (yellow: high intensity, black: low intensity). Horizontal line profiles taken at specific binding energies along the time (temperature) axis show the evolution of (g) Ni and (h) Fe intensities extracted from the corresponding heat maps in panels (d) and (e), respectively. (i) Ditto, for line profiles taken from the valence bands at E_F and at 1.5 eV (Fe²⁺) shown in panel (f).

the as-grown sample is composed of 3D metallic Ni clusters and free Fe₃O₄(001) surface with Ni¹⁺ adatoms and Ni²⁺ in near-surface octahedral sites. Emission from Ni⁰ from the bottom Ni layers in the 3D clusters and from the incorporated Ni²⁺ ions below the clusters is attenuated and therefore the overall Ni signal underestimates the amount of Ni present on the as-grown sample (see Sec. III).

The Fe 2p_{3/2} spectra [Fig. 3(e)] show a similar behavior as for the 1 ML deposition, but more pronounced. The Fe³⁺ to Fe²⁺ ratio is considerably reduced from 1.9 in the pristine sample to 1.2 in the as-grown sample (see Fig. SI8 [9]). As mentioned earlier, Fe³⁺ is enriched on the pristine reconstructed surface due to the subsurface cation vacancies [8]. Upon Ni deposition some Fe³⁺ is reduced to Fe²⁺ due to the Ni incorporation. Postannealing the sample up to 607 K recovers the spectral lineshape as Fe²⁺_{oct} in the subsurface region is replaced by Ni²⁺, whereby the intensities of the Fe²⁺ components are reduced. Concomitantly there is an overall decrease of Fe 2p_{3/2} intensity as the three-dimensional (3D) metallic Ni clusters disappear and Ni atoms spread out

evenly across the surface area and form a Ni ferrite-like surface compound. During the postannealing, cation diffusion is activated and subsurface octahedral sites are occupied by diffusing Ni atoms. VB spectra [Fig. 3(f)] show clearly the DOS of metallic Ni on the as-grown Ni film, which disappears after the postannealing, thus confirming our picture of 3D Ni clusters.

To track the kinetics of these processes, we performed temperature-dependent XPS. Figure 5 shows the evolution of the chemical states of nickel and iron in the near-surface and interface region during annealing as displayed in the Ni 2p_{3/2} [Fig. 5(d)] and Fe 2p_{3/2} [Fig. 5(e)] core-level spectra. The 26 ML deposition was reproduced with the same growth parameters to probe the changes in the VB region [Fig. 5(f)] during the same postannealing procedure with temperature-dependent UPS. The consistency of the two data sets is shown in Fig. SI9 [9]. In both cases the samples were heated in seven steps. The equilibrium temperatures of each ramp-up step are the same for the temperature-dependent XPS and UPS data sets, using slightly different time spans: One iteration

for temperature-dependent XPS, which included Ni $2p_{3/2}$, Fe $2p_{3/2}$, and O $1s$ (not shown in Fig. 5), corresponds to 6.8 min, while it is 7 min for temperature-dependent UPS. One single temperature step took nine iterations for temperature-dependent XPS, eight iterations for temperature-dependent UPS (see Fig. SI10 [9] for further details). Figures 5(a)–5(c) show the average temperature for each iteration together with the heat maps of Ni $2p_{3/2}$ [Fig. 5(d)], Fe $2p_{3/2}$ [Fig. 5(e)], and the VB region [Fig. 5(f)].

Figure 5(d) shows that Ni $2p_{3/2}$ has initially two distinct peaks located at 852.8 eV (Ni^0) and 854.9 eV (Ni^{2+}), as shown also in Fig. 3(d). Figure 5(g) shows the horizontal line profiles taken from the heat map at these two binding energies, displaying the changes in the spectral weight of the two nickel charge states with increasing temperature. The Ni^{2+} component decreases slightly between 423 K (iteration 25) and 523 K (iteration 47), while the Ni^0 signal starts to increase slightly just below 392 K (iteration 22) until the temperature reaches 473 K (iteration 37) (see zoomed-in graphs in Fig. SI11 [9]). At 473 K, the Ni^0 component starts to decrease, first gradually and then more steeply with a clear kink at about 563 K (iteration 57). This change in slope is mirrored in the steep increase of the Ni^{2+} component, as well as in the temperature-dependent intensity profile of the Fe^{2+} components of the Fe $2p_{3/2}$ spectrum [Fig. 5(h)], both of which reflect the progressing replacement of near-surface octahedral Fe^{2+} with Ni^{2+} ions.

The initial increase of the Ni^0 component suggests that the 3D Ni islands spread out laterally, thus reducing their initial thickness and thereby exposing more Ni^0 atoms in the top surface. This then explains the initial decrease of the Ni^{2+} component, because some of the areas of free $\text{Fe}_3\text{O}_4(001)$ surface with Ni^{1+} adatoms and Ni^{2+} in near-surface octahedral sites become covered with metallic Ni^0 . Interestingly, this process starts at a temperature well below the initial deposition temperature of 473 K. Taking into account that the deposition of 26 ML was done in 10.5 minutes, which corresponds to only 1.5 iterations in the temperature-dependent XPS data, this indicates that the dissolution of the 3D islands is kinetically hindered.

The valence-band heat map in Fig. 5(f) shows populated states up to E_F in the as-grown sample when the postannealing starts, due to the presence of 3D nickel islands. We examined the evolution of states at different binding energies as shown in Fig. 5(i): Ni^0 at 0 eV (E_F), and Fe^{2+} (e_g) at 1.5 eV [30]. The Fe^{2+} spectral intensity reaches a maximum at 423 K (iteration 25) and then drops off significantly, in concert with the corresponding component in the Fe $2p_{3/2}$ spectrum. The intensity at E_F peaks around 523 K (iteration 40), followed by a decay that contains a marked kink to a steeper slope, a behavior similar to what was found for the Ni^0 component in the Ni $2p_{3/2}$ spectra shown in Fig. 5(g). This behavior can be well understood within the scenario described in the preceding paragraph: The diffusion of Ni atoms from the 3D islands across the surface leads to an increase in the number of Ni^0 and Ni_{ad} atoms on the surface, before Ni atoms become incorporated into surface and subsurface octahedral sites. The change to a steeper slope may indicate that Ni incorporation into the cation vacancy sites has a lower activation energy than diffusion further into the subsurface [10].

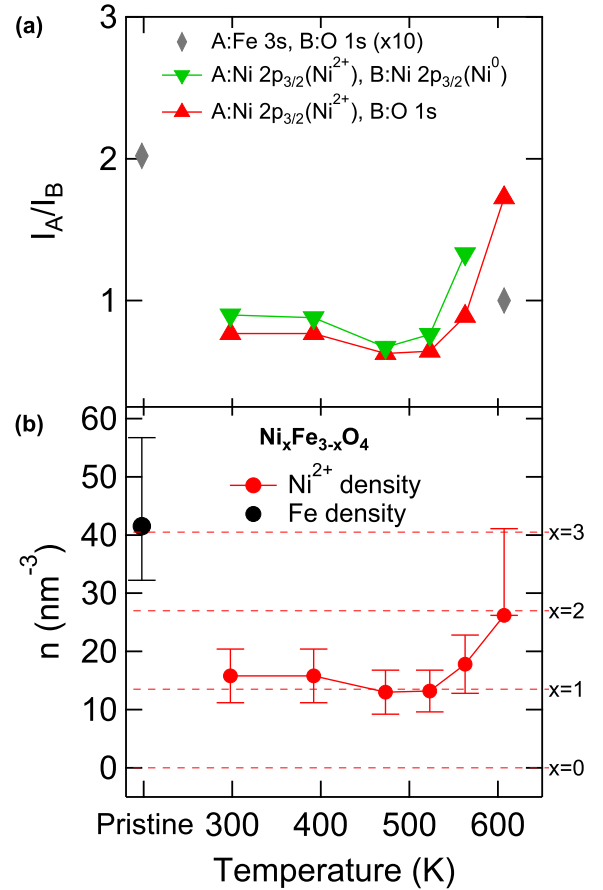


FIG. 6. Evolution of relative intensities and corresponding atomic densities with increasing temperature during postannealing. (a) Evolution of the XPS intensity ratios of Fe $3s$, to O $1s$ (gray diamonds), $\text{Ni}^{2+}2p_{3/2}$ to $\text{Ni}^02p_{3/2}$ (green downward triangles), and $\text{Ni}^{2+}2p_{3/2}$ to O $1s$ (red upward triangles). (b) Atomic density and the corresponding number of Ni^{2+} ions per unit cell volume (red circles) extracted from the intensity ratios shown in panel (a). The measured Fe density of the pristine sample is shown for comparison (black circle). The horizontal dashed lines denote the densities at which the metal to oxygen ratios have the values $x = 0, 1, 2, 3$. The error bars are obtained from the numerical analysis and are dominated by the uncertainty of the inelastic mean-free path (see text for details).

The accumulation of the excess Ni in metallic clusters and their dissolution during postannealing were studied more thoroughly using the numerical analysis outlined in Sec. III and shown in Figs. SI2 through SI6 [9]. The model considered the temperature-dependent spectral intensities from the substrate O $1s$, pre-existing nickel Ni^{2+} , and the clusters Ni^0 . The metallic Ni $2p_{3/2}$ spectrum in Fig. 3(g) was scaled to the XPS line cuts for various stages of growth (298, 392, 473, 523, 563 K) and postannealing (607 K) to determine the metallic contribution to the Ni $2p_{3/2}$ spectra in Fig. 5(d) (as seen in the waterfall representation in Fig. SI2 [9]). The Ni^0 spectra were subtracted from the Ni $2p_{3/2}$ spectra, with the remaining assigned to Ni^{2+} . However, it should be noted that a possible Ni^{1+} contribution cannot be distinguished in the Ni $2p_{3/2}$ spectra due to the dominance of the Ni^0 and

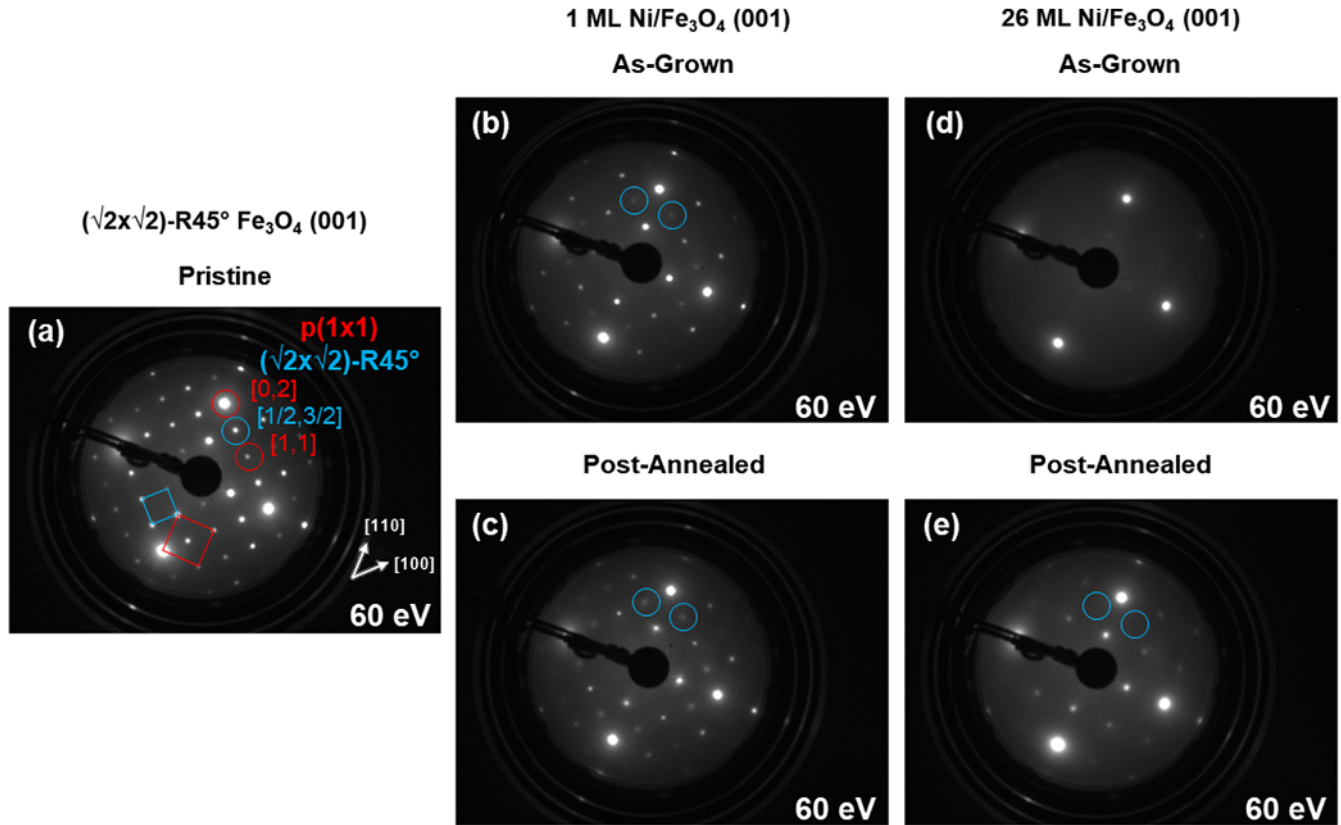


FIG. 7. LEED images taken at 60 eV for (a) pristine $\text{Fe}_3\text{O}_4(001)$ ($\sqrt{2} \times \sqrt{2}$ -R45°); (b), (c) and (d), (e) 1 ML and 26 ML $\text{Ni}/\text{Fe}_3\text{O}_4(001)$ samples, respectively, before and after postannealing. In panel (a) the reciprocal-lattice unit cells for reconstructed and bulk terminated surfaces are given in blue and red, respectively. LEED spots marked with blue circles indicate the presence of the $(\sqrt{2} \times \sqrt{2})$ -R45° surface reconstruction. Some LEED spots are labeled with respect to the $p(1 \times 1)$ reciprocal lattice vectors shown by the red square. The same grayscale was applied to all LEED images for the sake of consistency.

Ni^{2+} components. The intensity ratios of O 1s, Fe 2p, Ni^{2+} , and Ni^0 are shown in Fig. 6(a). The atomic density of nickel in $\text{Fe}_3\text{O}_4(001)$ ($n_{\text{Ni}^{2+}}$) was determined self-consistently using Eqs. (5) and (6) for each specified temperature and including corrections for photoelectron diffraction effects (as shown in Figs. SI3–SI6 [9]). Note that the error propagation in Fig. 6(b) was calculated using the reported uncertainty in the TPP-2M IMFP predictive formula for inorganic compounds, which is 18.9% [38]. The $n_{\text{Ni}^{2+}}$ was found to be near $x = 1$ up to 523 K, approaching a NiFe_2O_4 composition in (S-0) and (S-2) layers. However, above 523 K the $n_{\text{Ni}^{2+}}$ increases steeply as Ni clusters are dissolved and Ni atoms diffuse into the substrate. In the final stage of postannealing, a significant amount of Ni atoms become incorporated into the subsurface. This results in a near-surface composition close to $x \approx 2$ ($n_{\text{Ni}^{2+}} = 26.2^{+14.9}_{-0.0} \text{ nm}^{-3}$), which is substantially above the Ni density in nickel ferrite. This suggests that some Ni atoms near the surface may be in the 3+ oxidation state, although this could not be clearly distinguished in the XPS measurements. The density of atomic Fe in the pristine sample (n_{Fe}^0) was determined using the intensity ratio between the Fe 3s and O 1s peaks taking photoelectron diffraction effects into account (see Sec. III). This way, we retrieve $n_{\text{Fe}}^0 = 41.5^{+15.2}_{-9.3} \text{ nm}^{-3}$ from the XPS data, which is very close to the nominal value of $n_{\text{Fe}}^{\text{nom}} = 39.9 \text{ nm}^{-3}$ for the composition Fe:O = 3:4.

We now underlay the previous discussion with structural information obtained from low-energy electron diffraction (LEED) and XPD data. Figure 7 shows the LEED images obtained with 60 eV electron energy taken before and after postannealing the $\text{Ni}/\text{Fe}_3\text{O}_4(001)$ ($\sqrt{2} \times \sqrt{2}$ -R45° surfaces with 1 and 26 ML coverages. The overlaid squares on the pattern of the pristine sample in Fig. 7(a) refers to the characteristic $(\sqrt{2} \times \sqrt{2})$ -R45° pattern of the reconstructed surface (blue), plotted together with bulk truncated $p(1 \times 1)$ unit cell (red). Note that the $p(1 \times 1)$ cell is oriented along the $\{110\}$ direction, while the $(\sqrt{2} \times \sqrt{2})$ -R45° cell is oriented along the $\{100\}$ direction. Four much brighter spots dominate the LEED patterns. They reflect the periodicity of 2.96 \AA of the oxygen lattice along the $\{110\}$ directions, while the weaker spots in between represent the periodicities of lattice sites occupied with iron atoms (see Fig. SI1 [9]). Note that the fourfold symmetry of the LEED pattern results from the existence of two orthogonal domains of twofold surface terminations introduced by the presence of steps. As shown with blue circles in Figs. 7(b) and 7(c), the spots due to the $(\sqrt{2} \times \sqrt{2})$ -R45° reconstruction become fainter when the Ni coverage is 1 ML. This indicates that the subsurface cation vacancies in the (S-2)nd layer, which are present in the reconstructed surface, are partially filled with Ni.

At 26 ML Ni coverage, the as-grown LEED pattern shows no evidence of neither the $p(1 \times 1)$ nor the $(\sqrt{2} \times \sqrt{2})$ -R45°

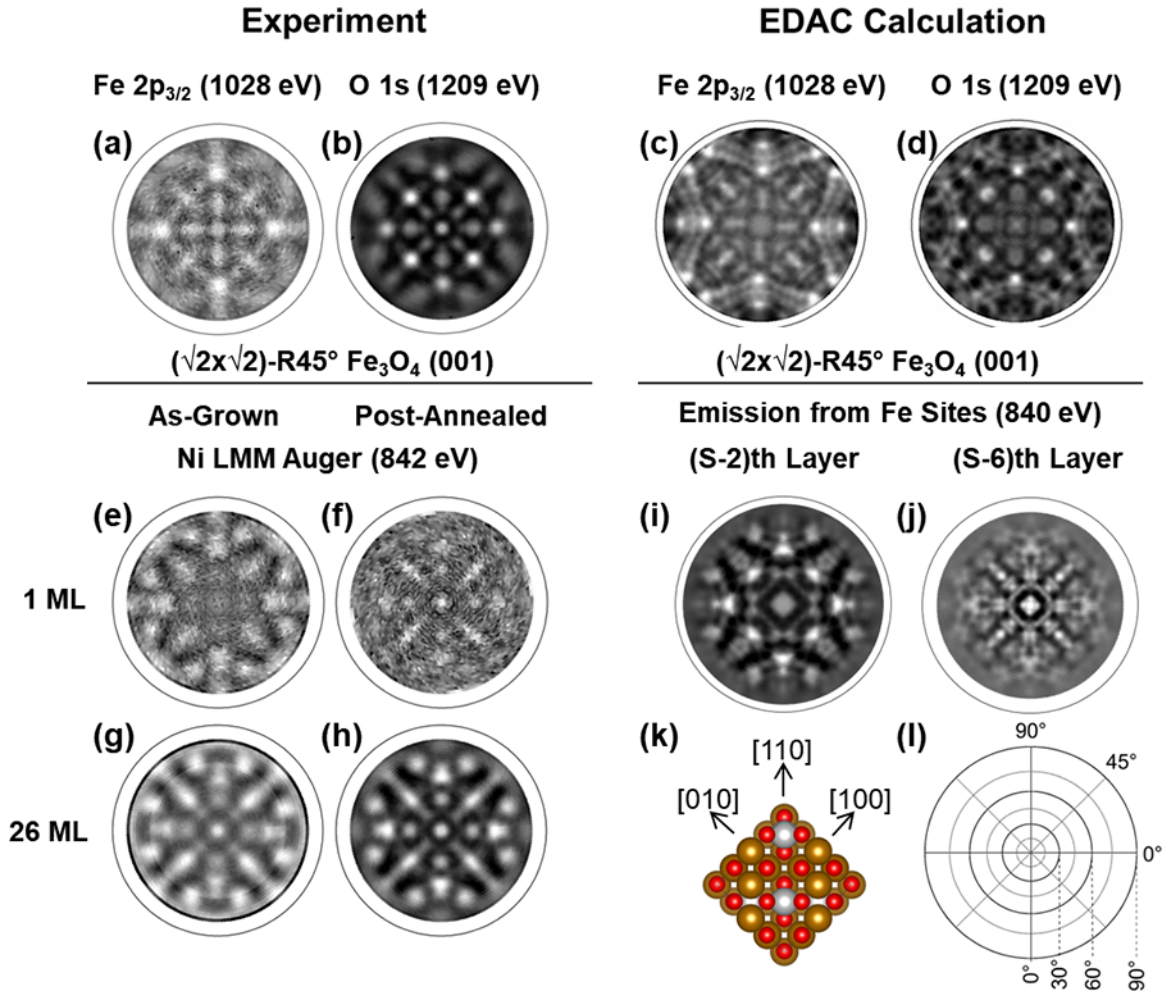


FIG. 8. Experimental (left panel) and simulated (right panel) XPD patterns. The kinetic energies of the photoelectrons are indicated. (a) Fe $2p_{3/2}$ and (b) O $1s$ XPD patterns measured on the reconstructed pristine sample and the corresponding EDAC simulations in panels (c) and (d), respectively. (e), (f) and (g), (h) Ni LMM Auger-electron diffraction patterns measured before and after postannealing for 1 ML and 26 ML Ni/ $\text{Fe}_3\text{O}_4(001)$ samples, respectively. EDAC simulations for Fe emission from Fe sites with the Ni LMM kinetic energy from (i) the (S-2)nd and (j) the (S-6)th layer. (k) The top view of $\text{Fe}_3\text{O}_4(001)$ unit-cell model illustrates the crystal orientation for the XPD patterns. (l) Angular grid of the XPD patterns in stereographic projection. X-ray sources: Nonmonochromatized Mg K_α excitation for Ni LMM Auger electrons; Nonmonochromatized Si K_α ($\hbar\omega = 1740$ eV) for Fe $2p_{3/2}$ and O $1s$ core levels.

lattice periodicities. The four bright spots persist, although. In the light of the scenario discussed above, this suggests that this pattern results from the surface areas free of 3D Ni islands. The absence of spots related to the cation periodicities further indicates that the Ni adatoms and incorporated Ni ions are randomly distributed on their respective lattice sites. Only very faint $p(1 \times 1)$ spots along $[110]$ and its fourfold symmetric directions are observed that would correspond to the periodicity of the rows along which the Ni_{ad} atoms adsorb. We have simulated a simple two-dimensional $p(1 \times 1)$ substrate model including randomly placed Ni atoms at different coverages on the topmost layer (see Fig. S112 [9]). The two-dimensional fast Fourier transform (2D-FFT) of the model indicates that Ni adsorption causes a significant intensity loss along $[1\bar{1}0]$ due to the loss of periodicity of the $\text{Fe}_{\text{oct}}(\text{S})$ rows, while the periodicity along $[110]$ rows remains robust. Postannealing of the sample causes the diffusion of Ni into the subsurface, resulting in a Ni ferrite-like structure and the corresponding

$p(1 \times 1)$ periodicity analogous to bulk terminated $\text{Fe}_3\text{O}_4(001)$ [see Fig. 7(e)].

XPD, an angle-resolved mode of XPS, is a useful technique for determining the local structural environment of specific elements on and near the surface. This technique is based on the diffraction patterns produced by photoelectrons excited from a particular emitter atom type and after scattering off the neighboring atoms. At photoelectron kinetic energies of a few hundred electron-volt, this scattering is strongly enhanced along the forward direction and produces characteristic intensity maxima along emitter-scatterer directions. It can therefore provide direct information about lattice sites of specific emitter atoms [23,24]. We first performed XPD measurements taken from pristine $\text{Fe}_3\text{O}_4(001)$ with Si K_α excitation. Figures 8(a) and 8(b) show the XPD patterns of Fe $2p_{3/2}$ and O $1s$, respectively. Both XPD patterns exhibit forward-scattering maxima in a fourfold symmetric arrangement. However, compared with O $1s$ the Fe $2p_{3/2}$ emission

shows a more diffuse pattern because Fe_{oct} and Fe_{tet} atoms occupy nonequivalent lattice sites in the crystal while oxygen atoms form a nearly regular face-centered cubic lattice. Moreover, there is a periodic undulation of the lattice sites in the top surface in response to the cation vacancies in the $(\sqrt{2} \times \sqrt{2})\text{-R}45^\circ$ reconstructed surface [8]. To further understand these effects, EDAC calculations were performed for both the reconstructed [Figs. 8(c) and 8(d)] and the bulk truncated surfaces (Fig. SI13 [9]). Simulations for these two surfaces show indeed that the reconstruction introduces a certain fuzziness in the two XPD patterns, which is much more pronounced in the Fe $2p_{3/2}$ emission. Overall, our XPD measurements on the pristine sample are consistent with the calculations for the reconstructed surface, with R factors of 0.36 and 0.35 for Fe $2p_{3/2}$ and O $1s$ emission, respectively, while the bulk-truncated surface yields R factors of 0.53 and 0.45, respectively.

As-grown and postannealed 1 and 26 ML Ni films on the reconstructed $\text{Fe}_3\text{O}_4(001)$ surface are examined with XPD measurements and EDAC calculations for further characterization [Figs. 8(e)–8(j)]. Ni LMM Auger emission excited by means of nonmonochromatized Mg K_α was used to determine the particular sites occupied by Ni atoms after the different preparation conditions. For 1 ML, the XPD pattern taken from the as-grown film shows a fourfold symmetric arrangement around Ni emitters [Fig. 8(e)]. We observe that the intensity modulation is more pronounced at large polar angles, i.e., close to 80° , than near normal emission in the center of the XPD pattern. Recalling the core-level spectrum of Fig. 3(a), as-grown Ni atoms are likely to occupy two different sites: adatom (Ni^{1+}) and octahedral (Ni^{2+}) sites. Being situated outside the top layer of $\text{Fe}_3\text{O}_4(001)$, adatoms will not contribute any forward-scattering maxima to the pattern. By comparison to layer-resolved EDAC simulations for Ni ions placed in octahedral sites (see Fig. 9) we can conclude that the majority of Ni ions reside in octahedral sites of layer (S-2) [Fig. 8(i)]. This suggests that, beside adatom sites, Ni atoms can occupy the subsurface cation vacancy sites of the reconstructed surface already at room temperature, which is in agreement with a recent x-ray standing wave (NIXSW) study, where a range of adsorption sites within the surface region was reported including subsurface vacancy sites [11]. There appear also considerable contributions from Ni atoms in surface (S-0) octahedral sites, as suggested by the enhanced intensity near grazing emission and at 45° in azimuthal angle [see Fig. 9(a)]. Interestingly, postannealing changes the pattern completely [see Fig. 8(f)]. A rather good match is seen with the EDAC simulation for emission from layers (S-4) and even (S-6), providing strong evidence that the Ni atoms diffuse away from the surface and deeper into the bulk of the crystal. It is consistent with the core-level spectra of Fig. 3(a), where we observe that postannealing leaves all Ni atoms in the Ni^{2+} state with attenuated emission. The results from the postannealed 1 ML Ni/ $\text{Fe}_3\text{O}_4(001)$ also match with the NIXSW measurements: The authors conclude that with increasing annealing temperature more Ni atoms diffuse from adatom sites into the subsurface region leaving adatom sites empty [11].

For 26 ML deposition, the higher growth temperature and the higher amount of Ni lead to a more pronounced Ni LMM

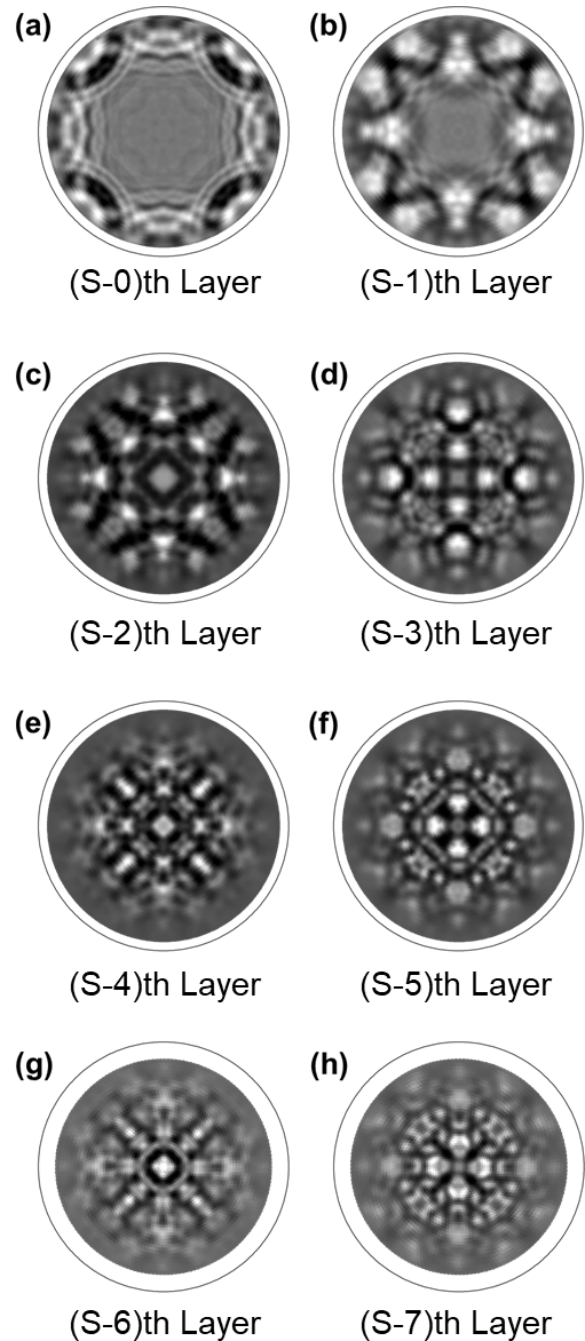


FIG. 9. Calculated XPD patterns for Fe emitters from the (S- n)th layer (from $n = 0$ to $n = 7$) with the Ni LMM Auger electron kinetic energy (840 eV). Layers with n even contain emitters on octahedral sites, those with n odd emitters on tetrahedral sites.

XPD pattern than for the 1 ML case already in the as-grown state [Fig. 8(g)], with characteristic features near the center of the pattern that indicate Ni incorporation already over several layers. Postannealing removes more ill-defined features present in the as-grown patterns at large emission angles and leads to a general sharpening of the pattern. Comparison with the layer-resolved EDAC simulations (see Fig. 9) the XPD pattern provides clear evidence for the occupation of octahedral sites over many layers in a Ni ferrite-like manner. Unlike in the case of the 1 ML Ni deposition we do not observe diffusion

of Ni away from the surface, but rather a stabilization of a Ni ferrite-like structure within the selvedge region, which is also confirmed by the $\text{Ni } 2p_{3/2}$ spectrum of Fig. 3(d).

V. CONCLUSION

In conclusion, the formation of $\text{Ni}_x\text{Fe}_{3-x}\text{O}_4$ on reconstructed $\text{Fe}_3\text{O}_4(001)$ surfaces was examined with surface characterization methods under UHV conditions. XPS measurements taken on as-grown 1 ML $\text{Ni}/\text{Fe}_3\text{O}_4(001)$ at room temperature showed two distinct chemical states: Ni^{1+} and Ni^{2+} correspond to Ni adatoms and incorporated Ni atoms, respectively. Postannealing the samples up to 607 K activates the diffusion of Ni adatoms towards the bulk of the crystal. XPD measurements showed that the deposition at room temperature already activates the incorporation process of Ni as they occupy octahedral sites in the (S-2)nd subsurface layer. The diffusion of Ni atoms with the postannealing takes them further into the bulk of the substrate with strong contributions from the (S-4)th and (S-6)th layers.

Moreover, 26 ML Ni were deposited on $\text{Fe}_3\text{O}_4(001)$ crystals at 473 K. On the as-grown sample we observe Ni in the oxidized Ni^{2+} and metallic Ni^0 chemical states. The incorporation of the excess atoms from metallic islands was monitored with temperature dependent XPS and UPS. The

diffusion towards the bulk of the crystal occurs in two steps: already incorporated Ni^{2+} in the first octahedral layers diffuse further into the bulk up to 463 K, as they are leaving their initial lattice sites at the subsurface for extra Ni atoms provided by metallic Ni clusters and Ni^{1+} adatoms at the surface. Even though continued incorporation of extra Ni atoms exceeds the composition of Ni ferrite (NiFe_2O_4 , $x = 1$) at 607 K, the XPD measurements taken after postannealing showed that Ni atoms continue to occupy octahedral sites in a well ordered spinel-type lattice in the subsurface region. A noteworthy result of this study on the $\text{Ni}/\text{Fe}_3\text{O}_4(001)$ model system is that there appears to be a critical amount of Ni deposition on the surface that is necessary to stabilize a Ni ferrite-like phase with excess Ni at the surface that makes an excellent catalyst. Lower amounts of Ni deposits seem to just diffuse into the bulk and disappear from the surface.

ACKNOWLEDGMENTS

This project has been funded under the University Research Priority Program - Light to Chemical Energy Conversion (URPP-LightChEC) of the University of Zurich. The authors thank Prof. Thomas Greber and Prof. Gareth Parkinson for fruitful discussions.

- [1] J. W. Ager, M. R. Shaner, K. A. Walczak, I. D. Sharp, and S. Ardo, Experimental demonstrations of spontaneous, solar-driven photoelectrochemical water splitting, *Energy Environ. Sci.* **8**, 2811 (2015).
- [2] E. Casbeer, V. K. Sharma, and X. Z. Li, Synthesis and photocatalytic activity of ferrites under visible light: A review, *Sep. Purif. Technol.* **87**, 1 (2012).
- [3] D. H. Taffa, R. Dillert, A. C. Ulpe, K. C. L. Bauerfeind, T. Bredow, D. W. Bahnemann, and M. Wark, Photoelectrochemical and theoretical investigations of spinel type ferrites ($\text{M}_x\text{Fe}_{3-x}\text{O}_4$) for water splitting: A mini-review, *J. Photonics Energy* **7**, 012009 (2017).
- [4] D. Hong, Y. Yamada, T. Nagatomi, Y. Takai, and S. Fukuzumi, Catalysis of nickel ferrite for photocatalytic water oxidation using $[\text{Ru}(\text{bpy})_3]^{2+}$ and $\text{S}_2\text{O}_8^{2-}$, *J. Am. Chem. Soc.* **134**, 19572 (2012).
- [5] F. Mirabella, M. Müllner, T. Touzalin, M. Riva, Z. Jakub, F. Kraushofer, M. Schmid, M. T. Koper, G. S. Parkinson, and U. Diebold, Ni-modified $\text{Fe}_3\text{O}_4(001)$ surface as a simple model system for understanding the oxygen evolution reaction, *Electrochim. Acta* **389**, 138638 (2021).
- [6] C. Haavik, S. Stølen, H. Fjellvåg, M. Hanfland, and D. Häusermann, Equation of state of magnetite and its high-pressure modification: Thermodynamics of the Fe-O system at high pressure, *Am. Mineral.* **85**, 514 (2000).
- [7] E. J. Verwey and P. W. Haayman, Electronic conductivity and transition point of magnetite (" Fe_3O_4 "), *Physica* **8**, 979 (1941).
- [8] R. Bliem, E. McDermott, P. Ferstl, M. Setvin, O. Gamba, J. Pavelec, M. A. Schneider, M. Schmid, U. Diebold, P. Blaha, L. Hammer, and G. S. Parkinson, Subsurface cation vacancy stabilization of the magnetite (001) surface, *Science* **346**, 1215 (2014).
- [9] See Supplemental Material at <http://link.aps.org/supplemental/10.1103/PhysRevMaterials.7.055801> for atomic structure of the pristine surface, XPS and LEED data analyses, experimental details about temperature-dependent measurements, reproducibility of the sample preparation, and additional XPD data, which includes Refs. [8,10,18,25,31,38].
- [10] R. Bliem, J. Pavelec, O. Gamba, E. McDermott, Z. Wang, S. Gerhold, M. Wagner, J. Osiecki, K. Schulte, M. Schmid, P. Blaha, U. Diebold, and G. S. Parkinson, Adsorption and incorporation of transition metals at the magnetite $\text{Fe}_3\text{O}_4(001)$ surface, *Phys. Rev. B* **92**, 075440 (2015).
- [11] P. T. Ryan, Z. Jakub, J. Balajka, J. Hulva, M. Meier, J. T. Küchle, P. J. Blowey, P. K. Thakur, C. Franchini, D. J. Payne, D. P. Woodruff, L. A. Rochford, F. Allegretti, T. L. Lee, G. S. Parkinson, and D. A. Duncan, Direct measurement of Ni incorporation into $\text{Fe}_3\text{O}_4(001)$, *Phys. Chem. Chem. Phys.* **20**, 16469 (2018).
- [12] R. Bliem, R. Kosak, L. Perneczky, Z. Novotny, O. Gamba, D. Fobes, Z. Mao, M. Schmid, P. Blaha, U. Diebold, and G. S. Parkinson, Cluster nucleation and growth from a highly super-saturated adatom phase: Silver on magnetite, *ACS Nano* **8**, 7531 (2014).
- [13] Z. Novotný, G. Argentero, Z. Wang, M. Schmid, U. Diebold, and G. S. Parkinson, Ordered Array of Single Adatoms with Remarkable Thermal Stability: $\text{Au}/\text{Fe}_3\text{O}_4(001)$, *Phys. Rev. Lett.* **108**, 216103 (2012).
- [14] G. S. Parkinson, Z. Novotny, G. Argentero, M. Schmid, J. Pavelec, R. Kosak, P. Blaha, and U. Diebold, Carbon monoxide-induced adatom sintering in a $\text{Pd}-\text{Fe}_3\text{O}_4$ model catalyst, *Nat. Mater.* **12**, 724 (2013).
- [15] X. Shi, Y. F. Li, S. L. Bernasek, and A. Selloni, Structure of the $\text{NiFe}_2\text{O}_4(001)$ surface in contact with gaseous O_2 and water vapor, *Surf. Sci.* **640**, 73 (2015).

- [16] R. S. Saiki, A. P. Kaduwela, M. Sagurton, J. Osterwalder, D. J. Friedman, C. S. Fadley, and C. R. Brundle, X-ray photoelectron diffraction and low-energy electron diffraction study of the interaction of oxygen with the Ni(001) surface: $c(2 \times 2)$ to saturated oxide, *Surf. Sci.* **282**, 33 (1993).
- [17] W.-D. Zabka, M. Mosberger, Z. Novotny, D. Leuenberger, G. Mette, T. Kälén, B. Probst, and J. Osterwalder, Functionalization and passivation of ultrathin alumina films of defined sub-nanometer thickness with self-assembled monolayers, *J. Phys.: Condens. Matter* **30**, 424002 (2018).
- [18] J. H. Scofield, Hartree-Slater subshell photoionization cross-sections at 1254 and 1487 eV, *J. Electron Spectrosc. Relat. Phenom.* **8**, 129 (1976).
- [19] S. Tanuma and C. J. Powell, Electron inelastic mean free paths. 5. Data for 14 organic-compounds over the 50–2000 eV range, *Surf. Interface Anal.* **21**, 165 (1994).
- [20] J. Osterwalder, T. Greber, S. Hüfner, and L. Schlapbach, Photoelectron diffraction from core levels and plasmon-loss peaks of aluminum, *Phys. Rev. B* **41**, 12495 (1990).
- [21] M. P. Seah, I. S. Gilmore, and G. Beamson, XPS: Binding energy calibration of electron spectrometers 5—re-evaluation of the reference energies, *Surf. Interface Anal.* **26**, 642 (1998).
- [22] T. J. Kreutz, T. Greber, P. Aebi, and J. Osterwalder, Temperature-dependent electronic structure of nickel metal, *Phys. Rev. B* **58**, 1300 (1998).
- [23] C. S. Fadley, The study of surface structures by photoelectron diffraction and Auger electron diffraction, in *Synchrotron Radiation Research: Advances in Surface and Interface Science Techniques*, edited by R. Z. Bachrach (Springer US, Boston, 1992), pp. 421–518.
- [24] J. Osterwalder, Structural effects in XPS and AES: Diffraction, in *Surface Analysis by Auger and X-Ray Photoelectron Spectroscopy*, edited by D. Briggs and J. Grant (IM Publications and Surface Spectra Limited, Manchester, 2003), p. 557.
- [25] F. J. García de Abajo, M. A. Van Hove, and C. S. Fadley, Multiple scattering of electrons in solids and molecules: A cluster-model approach, *Phys. Rev. B* **63**, 075404 (2001).
- [26] D. Naumović, A. Stuck, T. Greber, J. Osterwalder, and L. Schlapbach, Full-hemispherical photoelectron-diffraction data from Cu(001): Energy dependence and comparison with single-scattering-cluster simulations, *Phys. Rev. B* **47**, 7462 (1993).
- [27] J. B. Pendry, Reliability factors for LEED calculations, *J. Phys. C: Solid State Phys.* **13**, 937 (1980).
- [28] D. P. Woodruff and A. M. Bradshaw, Adsorbate structure determination on surfaces using photoelectron diffraction, *Rep. Prog. Phys.* **57**, 1029 (1994).
- [29] K. Momma and F. Izumi, VESTA 3 for three-dimensional visualization of crystal, volumetric and morphology data, *J. Appl. Crystallogr.* **44**, 1272 (2011).
- [30] J. Chen, D. J. Huang, A. Tanaka, C. F. Chang, S. C. Chung, W. B. Wu, and C. T. Chen, Magnetic circular dichroism in Fe 2*p* resonant photoemission of magnetite, *Phys. Rev. B* **69**, 085107 (2004).
- [31] A. P. Grosvenor, B. A. Kobe, M. C. Biesinger, and N. S. McIntyre, Investigation of multiplet splitting of Fe 2*p* XPS spectra and bonding in iron compounds, *Surf. Interface Anal.* **36**, 1564 (2004).
- [32] P. S. Maiya and J. M. Blakely, Surface self-diffusion and surface energy of nickel, *J. Appl. Phys.* **38**, 698 (1967).
- [33] M. H. Ri, U. S. Ri, Y. N. Kim, Y. S. Sin, and M. J. Chon, Adsorption characteristics of citric acid on Fe₃O₄ (001), (011), and (111) surfaces, *J. Mol. Model.* **27**, 332 (2021).
- [34] S. He, D. Ji, J. Zhang, P. Novello, X. Li, Q. Zhang, X. Zhang, and J. Liu, Understanding the origin of selective reduction of CO₂ to CO on single-atom nickel catalyst, *J. Phys. Chem. B* **124**, 511 (2020).
- [35] M. Lenglet, A. D’huysser, J. Bonelle, J. Dürr, and C. Jørgensen, Analysis of x-ray Ni K β emission, xanes, xps, Ni 2*p*, and optical spectra of nickel(II) spinels and structure inference, *Chem. Phys. Lett.* **136**, 478 (1987).
- [36] H. Magnan, P. Le Fèvre, D. Chandesris, P. Krüger, S. Bourgeois, B. Domenichini, A. Verdini, L. Floreano, and A. Morgante, Resonant photoelectron and photoelectron diffraction across the Fe *L*₃ edge of Fe₃O₄, *Phys. Rev. B* **81**, 085121 (2010).
- [37] H. Liu and C. Di Valentin, Band gap in magnetite above Verwey temperature induced by symmetry breaking, *J. Phys. Chem. C* **121**, 25736 (2017).
- [38] C. Powell and A. Jablonski, *NIST Electron Inelastic-Mean-Free-Path Database - Version 1.2* (National Institute of Standards and Technology, Gaithersburg, 2010).